Operando SAXS/WAXS on a-P/C as Anode for Na-ion Batteries

Mauro Povia,[a] Jonas Sottmann,[b] Giuseppe Portale,[c] Kenneth D. Knudsen,[d] Serena Margadonna[e] and Sabrina Sartori[f,*]

[a] *Department of Physics, University of Oslo, Blindern, P.O. Box 1048, 0316 Oslo, Norway*

[b] *Department of Chemistry, University of Oslo, Blindern, P.O. Box 1033, 0315 Oslo, Norway*

[c] *Zernike Institute for Advanced Materials, University of Groningen, Nijenborgh 4, 9747 AG, Groningen, The Netherlands*

[d] *Physics Department, IFE, P.O. Box 40, 2027 Kjeller, Norway*

[e] *College of Engineering, Swansea University, Swansea SA1 8PP, UK*

[f] *Department of Technology Systems, University of Oslo, P.O. Box 70, 2027 Kjeller, Norway*

*Corresponding author: e-mail: sabrina.sartori@its.uio.no

Abstract

A complete chemical and morphological analysis of the evolution of battery electrode materials can be achieved combining different and complementary techniques. *Operando* small-angle X-ray scattering (SAXS) and wide-angle X-ray scattering (WAXS) were combined to investigate structural and electrochemical performances of a Na-ion battery, with amorphous red phosphorus in carbon matrix (a-P/C) as the active anode material in a Swagelok type cell. The charging process results in the formation of crystalline Na_3P, while during discharging the anode material returns to the initial a-P/C. From the analysis of the WAXS curves the formation of crystalline phases appears only at the end of charging. However, SAXS data show that a partial re-organization of the material during charging occurs at length scales non-accessible with conventional X-ray diffraction, corresponding to a real space ordering distance of 4.8 nm. Furthermore, the analysis of the SAXS data shows that the electrode remains dense during charging, while it develops some porosity during the discharge

phase. The presented results indicate that the combination of SAXS/WAXS adopted simultaneously, and non-destructively, on a working electrochemical cell can highlight new mechanisms of reactions otherwise undetected. This method can be applied for the study of any other solid electrode material for batteries.

Introduction

Large-scale electric storage is required for the integration of renewable energy sources into the power grid. Considering the large quantity of active materials needed for the installation of such systems, sodium-ion batteries (SIB) are emerging as alternative to the lithium-based materials. Graphite is the negative electrode material currently utilized in lithium-ion batteries (with a specific capacity of 372 mAh/g), and researchers are seeking alternatives such as silicon or nano-structuring to improve the anode capacity.[1] With regards to anodes for SIBs there is a need to look for alternatives to what works for lithium-ion batteries because silicon does not reversibly store Na-ions at ambient conditions, and Na insertion in graphite is thermodynamically unfavorable, limiting capacities to 30-35 mAh/g.[2] A few electrode materials have been reported to be suitable for SIBs, such as metal oxides (200 mAh/g)[3] like iron-oxide[4] or titanium-oxide (70-189 mAh/g) [5,6] and ilmenite,[7] hard-carbon (300 mAh/g),[8] alloys (300-850 mAh/g, e.g.SnS_2/C,[9] SnSb/C,[10] $FeSb_2$[11]), [,11] carbon black,[12] and various MoS_2 morphologies (250-900 mAh/g).[13,14] Recently, it was demonstrated that amorphous carbon can also be used as anode for SIBs.[15] Recent studies reported the electrochemical performance of the black phosphorus, red phosphorus and amorphous red phosphorus in carbon matrix (a-P/C), showing that the latter achieved the best cycling performance, probably due to the carbon matrix improving the electron conductivity.[16,17,18] In most cases, these studies showed poor stabilities during cycling and/or incomplete reversibility. A breakthrough in the anode architectures is therefore needed to improve the cycle stability and Na^+ transport.

Elemental phosphorus has a theoretical specific capacity of 2596 mAh/g and combined with A = Li, Na, it forms the hexagonal (space group $P6_3/mmc$) A_3P alkaline compound. Along the *c*-axis the A^+ and the P^{3-} are forming two layers: one layer is composed of A^+ with a chair cyclohexane-like ring structure; the second layer is a graphite-like sheet of A^+ and P^{3-}.[19]

Operando diffraction techniques (X-ray or neutron-based), where the performance of the electrodes is constantly monitored inside a closed electrochemical

cell, are emerging as the desired fundamental methods of characterization for electrochemical cells. Some groups developed technical solutions to determine the crystalline components of the battery *operando*.[11,20,21,22,23] However, in many system, during the charge/discharge process the active material is amorphous. To improve the design of future commercial batteries we consider relevant to study in detail the formation and evolution of the amorphous phases with Small-angle X-ray scattering (SAXS). This is a very useful technique to investigate structural changes occurring at short-range, complementary to the longer-range order information obtained with wide-angle X-ray scattering (WAXS). Herein, we report the simultaneous acquisition of SAXS and WAXS data on a high-capacity amorphous anode for SIB during charge/discharge cycles. The advantage of this study lies in the possibility to monitor both particle nanoscale effects and phase transformation over a large range, without disassembling the cell. The cell[22] used in the study works in transmission mode, and the complex superimposed scattering data from the various components of the battery are carefully analyzed, also considering the individual contributions to the SAXS signal by detailed *ex-situ* measurements of each cell component. We demonstrate how the *operando* combination of multiple techniques can shed light on mechanisms taking place during cycling. The use of SAXS could also help to understand phenomena occurring at length scales outside the classical XRD range.

Experimental Section

The a-P/C nanocomposite was synthesized by high-energy ball milling of commercial red phosphorus powder (99.99%, Sigma Aldrich) with carbon black (Super P, Timcal) at a-P/C ratio of 7:3, for 24 hours and with balls-to-powder-ratio of 20:1. Ball milling was carried out with a Fritsch Pulverisette 7, at 750 rpm, under argon.

The anode was prepared by mixing the active material (80 wt.%) with 10 wt.% Super P and 10 wt.% mixture of polymer binders in water. The mixture of polymer binders was composed of two different kind of sodium carboxymethyl (CMC): 50 wt.% CMC M_w= 250,000 EW (Sigma Aldrich) and 50 wt.% CMC M_w = 700,000 EW (Sigma Aldrich). The as-prepared slurry was manually spread by a metal blade on an aluminum foil previously washed in methanol. The slurry was dried under vacuum in an oven at 60° C overnight (final thickness of the anode was about 20 μm).

A half-cell based on the a-P/C anode and metallic Na as counter electrode was assembled in an X-ray transparent Swagelok-type electrochemical cell using Kapton windows.[22] A glass fiber separator (Whatman, GF/C) was soaked with the electrolyte (1M $NaPF_6$ in EC:DEC (1:1 wt.%) with the addition of 5 wt.% of FEC, where EC = ethylene carbonate, DEC = diethyl carbonate, FEC = fluoro-ethylene carbonate. All chemicals were purchased from Sigma Aldrich).

The cell was used in transmission geometry with respect to the incoming X-ray beam. SAXS and WAXS were collected in parallel with the same cell at beamline BM26B at the European Synchrotron (ESRF) in Grenoble, France.[24,25] The wavelength was $\lambda = 0.82666$ Å (corresponding to an X-ray energy of 15 keV) and the beam size was 1.5 mm x 0.3 mm.

The SAXS detector was a Pilatus 1M placed at a distance of 130 cm from the sample. The calibration of the scattering vector was performed by using the diffraction peak position of a silver behenate standard powder sample. Standard corrections for background subtraction and sample transmission were applied. WAXS was recorded using a Pilatus 300K detector placed at a distance of 27 cm from the sample. The angular scale was calibrated using the position of diffracted rings from a standard alpha Al_2O_3 powder. Both SAXS and WAXS 2D images were integrated to produce 1D profiles by means of the python-based BUBBLE software package available at the beamline.[26]

While irradiating with X-rays, the cell was connected to a galvanostat (BatSMALL, Astrol) to measure the galvanostatic charge/discharge cycles at C/10. The exposure time used for both SAXS and WAXS images was 60 s and the exposure period was one image every two minutes (selections of measurements are shown in Figures S1, S2 and S3 of the Supplementary Information). *Ex-situ* SAXS and WAXS measurements of the different components of the cell were performed with the same wavelength and 60 s of exposure time (Figure S4 for the *ex-situ* SAXS).

Results and Discussion

During the high-energy ball milling the pristine phosphorus was broken into smaller clusters resulting in a homogeneous distribution of P in the carbon matrix (as confirmed by the EDX measurement, Figure S5). This leads to the formation of a-P/C. Nanoclusters of P increase their volume up to 308% during sodiation (corresponding to the charging process), with the molar volume of the Na_3P (57.4

cm^3/mol) being four times bigger than the molar volume of the red P (14.1 cm^3/mol).[17] In general, a large volume variation is a limiting factor for the performance of batteries,[27,28] because mechanical stress induced by large volume changes can decrease the electronic conductivity due to the loss of contact between the active material and the current collector. The carbon matrix in the a-P/C is proposed to reduce the mechanical stress during charge/discharge,[16,17] while its contribution to the specific capacity is negligible (173 mAh/g),[15] being 13 times lower than the theoretical capacity of P. Once the anode is prepared by milling, the thermally cross-linked three-dimensional interconnection of polymer binders, such as CMC, enhance the electrochemical performance of the phosphorus-based materials.[29,30]

Figure 1a shows the electrode potential vs. specific capacity in the *operando* set up SAXS/WAXS/galvanostat at ESRF. The variation of the anode potential is measured against Na^+/Na. The capacity for the first cycle reaches a value of 2000 mAh/g, near the theoretical value (2596 mAh/g) with a total reversible specific capacity of 1762 mAh/g (and a Coulomb efficiency of 85%). The charge profile of the battery is characterized by two slopes, at 1.0-0.4 V and 0.4-0.2 V, and a plateau at 0.2 V. The discharge profile has one plateau at 0.5 V and three slopes, at 0.6-0.8 V, 0.8-1.2 V, and 1.2-1.5 V, respectively. Due to the cell design and the transmission geometry, the X-ray beam penetrates the whole assembly, and scattering from all the different parts of the battery (anode, cathode, electrolyte, etc.) will contribute to the recorded SAXS and WAXS signal. It follows that data interpretation and analysis is challenging. However, Figures 1b and 1c show the evolution of the diffraction peaks (110) and (103) of crystalline Na_3P, as clearly visible in the d-range 2.5- 2.3 Å of the WAXS. Point A in the voltage profile (at 0.2 V of Figure 1a) corresponds to the initial formation of crystalline Na_3P of Figure 1b. The signal from Na_3P reaches maximum intensity at the end of the sodiation (charge) process (corresponding to point C in Figure 1a). During desodiation (discharge) the Na_3P peak intensity decreases (Figure 1c) until the complete disappearance at point E, corresponding to the potential value 1.5 V in Figure 1a. The Na and P phase diagram is composed of several amorphous and crystalline phases with different stoichiometry,[31] and only the crystalline Na_3P ($P6_3/mmc$) was detected with X-ray data. Qian *et al.*[16] proposed a possible desodiation path through the following stages: Na_3P, Na_2P, NaP, NaP_7, and P. However, recently Sottmann e*t al.*[32] suggested an alternative phase transition path

based on *operando* measurements combining pair distribution function (PDF), X-ray computer tomography (CT) and density function theory (DFT) calculation. The authors proposed the sodiation steps as follows: Na_2P_3, Na_3P_4, NaP, Na_5P_4, Na_4P_3, Na_3P. The desodiation steps are instead: Na_3P, $Na_{2.6}P$, $Na_{2.3}P$.

Due to the amorphous state of the active material in the initial and final stages of the charge/discharge cycle, WAXS data alone give incomplete structural information of the reactions taking place. Therefore, the simultaneous collection of SAXS data has been considered important to obtain additional information.

For simplicity, Figure 2a shows the SAXS curves at the beginning and the end of the charge/discharge cycle. Although after the desodiation process the phosphorus returns to its amorphous state, as indicated by WAXS, the SAXS measurements clearly show that the profile at the beginning of the measurement (black curve) is different from the profile after the charge/discharge cycle is completed (red curve). This indicates that the structural morphology of the samples is modified permanently after the first cycle. During the charging a signal, T, appears and increases (Figure 2c), while its intensity remains constant during discharge.

Interestingly, after point D of Figure 1a, the progressive desodiation corresponds to the appearance and growth of the new feature in the SAXS curves indicated as Z (Figure 2b). This sharp signal is likely to come from some type of superstructure in the sample. Beside the appearance of signals Z and T, also the intensity and the slope of the SAXS curves in the q-range 0.2-3/nm changes after discharge (Figure 2a). These phenomena are ascribed to the electrode evolution and are not related to a background shift, as any change in the background scattering also would produce a modification in the feature at q = 4/nm, corresponding to the kapton windows of the electrochemical cell used in the experiments. This peak is constant during the entire cycle, suggesting that no significant change in the background scattering occurs.

The measured intensity of a SAXS experiment, I(q), is a function of the electron density (ρ), expressed in form of the contrast factor $\Delta\rho^2$:

$$I(q) = K\Delta\rho^2 \, P(q)S(q)$$

where K is a specific constant, P(q) is the form factor function for the shape of the scattering particles, while the structure factor S(q) describes the distribution of the particles in space and inter-particle interactions. In the present study, the scattered

intensity derives from a superposition of the various components of the battery considered as independent scattering systems. The *ex-situ* SAXS measurements performed on the single components (Figure S4 of the supplementary information) and on the blank are compared to the intensity from the assembled battery. The major scattering contribution can be attributed to the scattering from the active material of the anode (a-P/C + CMC + CSP), while the cell without the active material gives minor contribution to the total scattering at low angles.

If we focus first on the SAXS pattern (Figure 2a) below the main diffraction peaks, i.e. below ca. 2/nm, at least two different Porod-like ranges can be observed (close to straight lines in a log-log plot), plus a central region with a bump, indicative of a characteristic size – on the order of a few nanometers – present in the system. This means that it may be reasonable to use a global unified function (Beaucage model) for fitting the overall pattern in this q-range.[33] However, the absence of a plateau at low q-values in Figure 2a indicates that in addition to the small structures mentioned above, there are also some much larger entities present. These are so large that we only see the tail, i.e. a Porod-region, with a certain log-log slope (approx. -4). Thus, we have at least a two-level hierarchical system, and need (at least) a 2-level Beaucage model to represent the whole pattern.

With this method, we obtained a reasonable fit of the SAXS curve for the initial situation (Figure 3a). Here the slope (α) in the low-q region is -4, representing the tail of some very large entities (the size of which was set arbitrarily to a large value, 50 nm, so that no plateau could be observed in the model curve). The surface fractal exponent is generally equal to 6 - $|\alpha|$, which here results in a value of 2, thus these structures have a nearly smooth surface. The smaller entities could now be extracted more reliably from the mid-q range, giving an average radius of gyration $R_g = 3$ nm. If we assume that this characteristic size represents (on average) spherically-shaped particles, since the pattern does not seem to indicate otherwise, e.g. rod-like or disk-like particles, the average particle size is $D = 2\ (5/3)^{1/2}\ R_g = 7.7$ nm. The weak signal in Figure 3a at ca. 2.5/nm is ascribed to a residual Kapton windows contribution, rather than a real structure.

A similar analysis at the end of the desodiation is shown in Figure 3b. The pattern has changed considerably with respect to the initial state. Apart from the additional small feature at ca. q = 1.3/nm, there is a clear change in the low-q slope.

At the end of desodiation the low-q slope is found to be ca. -2.5. This indicates a very open structure, characteristic of a mass fractal system (with theoretical maximum value of 3). This is in strong contrast to the smooth surfaces encountered before sodiation.

The SAXS patterns can thus be explained by a physical system with at least one characteristic size around R_g = 3 nm. The diffraction peak (peak Z in Figure 2) appearing at ca. q = 1.3/nm, corresponds to a real space ordering distance of $2\pi/1.3$ = 4.8 nm. Thus, we can conclude that there is some regular ordering emerging in the system towards the end of the desodiation. It is possible that the increased surface roughness found is related to the structures that organize with this repeating distance of 4.8 nm.

The Beaucage fitting performed on a number of SAXS curves showed that during sodiation there is no change in R_g, and the low-q slope is nearly constant over the whole range. This is confirmed by visual inspection of the SAXS curves reported every 100 mAh/g (Figure S2). The same analysis was performed during desodiation. Also in this case, the fitted R_g remains unchanged (within uncertainty). However, it was found that the low-q slope changes systematically, as shown in Figure 4a. The large decrease around ca. 800 mAh/g (during desodiation) corresponds to a change from a system with rough internal surfaces (slope slightly above 3.0) to a more open mass fractal-like system, as mentioned earlier.

Information about the volume fraction of the particles in the sample can be obtained via the so-called Porod invariant, q*. The latter is given as the intensity multiplied by the square of the scattering vector modulus, integrated over the full q-range, $q^* = \int I(q)\, q^2\, dq$. By considering the total q-range, the invariant is independent of the size and shape of the particles, and depends only on volume fraction (and specific surface). Here we want to relate the variation of integrated intensity with the sodiation/desodiation curves to make a link with the electrochemical results. The integration at each specific capacity goes from zero to infinity in q, thus extrapolation of the intensity curves in the low- and high-q limit of the SAXS data was first made.[34] The volume fraction φ can now, in principle, be calculated from the expression $\varphi(1-\varphi) = q^*/(2\pi\Delta\rho^2)$, where Δρ is the difference in scattering length density.[35] It should be mentioned, however, that this formalism is strictly applicable only for a two-phase

system (homogeneous particles in a matrix) and assumes that the density (and thus contrast) does not vary during the process. This is a simplification of the current system, since there are likely to be phase transformations that can modify the contrast. On the other hand, we prefer to present these data in order to look for correlations that can help understanding the process, taking into account that one has to be cautions with the interpretation. The contrast factor ($\Delta\rho$) is not known a priori, but can be estimated to be in the order of 1e-06/Å^2 (see calculation further down). Employing this value, we can get a nominal (apparent) volume fraction as output in order to follow the trends. Table 1 shows the calculated values of this volume fraction for selected stages of sodiation/desodiation.

Table 1 Volume fraction percentages at each corresponding specific capacity value

	Sodiation		**Desodiation**					
Situation	**Start**	**End**	**Start**					**End**
Capacity (mAh/g)	0	2000	2000	1481	1173	772	471	246	0
Vol. frac.(%)	0.11	0.15	0.15	0.15	0.16	0.17	0.27	0.26	0.26

During sodiation, we observe only a small increase of the apparent volume fraction, i.e. from the entities that contribute to the SAXS signal. This can be traced back to the slight changes in the SAXS patterns during sodiation and at the beginning of desodiation. Instead, there is a larger change in this value during the process of desodiation, shown graphically in Figure 4b. This can clearly be identified when inspecting the SAXS data, where it is noted that the patterns are shifted upwards considerably around 800 mAh/g (Figure S3). After this point and towards the end of the desodiation, the situation is more stable, as can also be seen from the values of the apparent volume fraction (ca. 0.26 in Table 1 and Figure 4b). This behavior correlates well with the observations of the low-q behavior for the power law shown in Figure 4a, i.e. a drastic change around 800 mAh/g. Thus, the behavior is systematic, although it may be difficult to identify exactly the underlying nanostructural rearrangements.

By integrating the area under the feature at 4.7/nm (T in Figure 2a) for SAXS curves during sodiation, every 100 mAh/g, we see a continuous increase in the value until a distinct jump after 1600 mAh/g (Figure 5). Instead, the feature marked Z

grows only in the final part of the desodiation process (it is too weak to make a proper integration), but the position, corresponding to a distance of 4.8 nm, is likely to reflect a crystalline-like structure being built up. During cycling, chemical reactions occur between the sodium cation and the active material. According to previous reports, there are two important phenomena involving the metallic sodium counter electrode: 1) the formation of sodium dendrite (during desodiation) and 2) the instability of the SEI when carbonate solutions are used as electrolyte,[36,37] as in our experimental set up. These could explain the stability of the feature T during desodiation, and the fluctuation of the feature Z in our study.

We will now discuss how the scattering contrast factor is changing during the Na sodiation/desodiation in the active material (a-P/C anode). Calculation of contrast requires the knowledge of the X-ray scattering length densities (SLD) in the system. The SLD can be estimated knowing the chemical composition of the particle/entity and the mass density ρ_m (g/cm^3). The latter can be calculated from the specific volume V_m (cm^3/mol) together with the molecular weight M_w, i.e. $\rho_m = M_w / V_m$. The specific volume for Na_3P is known to be 57.4 cm^3/mol, and employing the M_w of Na_3P of 100 g/mol, this corresponds to a mass density of 1.74 g/cm^3. Therefore, we can calculate an SLD for Na_3P of 1.42e-05/Å^2. The specific volume for nanoclusters of P is much smaller, 14.1 cm^3/mol, corresponding to a mass density of 2.21 g/cm^3. This results in an SLD of 1.83e-05/Å^2. Estimating the mass density of Na_2P and NaP from interpolation between the fully sodiated (Na_3P) and fully desodiated (P) phosphorus, we obtain mass densities for these as 1.90 and 2.05 g/cm^3, respectively. This finally gives SLD-values of 1.56e-05/Å^2 and 1.69e-05/Å^2 for these two phases, as shown in Table 2.

Table 2 SLD and ρ_m for different Na_xP compounds

Compound	**Na_3P**	**Na_2P**	**NaP**	**P**
ρ_m (g/cm^3)	1.74	1.90	2.05	2.21
SLD (1/Å^2)	1.42e-05	1.56e-05	1.69e-05	1.83e-05

The difference in SLD between the various sodiation states of the phosphorus is therefore quite small, with the pure phosphorus presenting a relatively larger contrast with respect to any surrounding voids (SLD = 0) than the partly or fully sodiated entities (cf. Table 2). However, from the SLD values it is clear that none of these compounds will give a dominating scattering signal with respect to the others if they

co-exist in the same scattering volume. Therefore, the individual contributions from each of these to the overall signal cannot easily be quantified. On the other hand, one can see from this calculation that any gradual conversion from a fully sodiated system (Na_3P) towards a desodiated system (P) results in an increased SLD, and thus a continuously larger scattering contrast with respect to low-density surroundings (or voids). This could explain the gradual increase in scattering signal observed during desodiation. It is then interesting that such a change is not observed during sodiation. Here the change is only seen in the SAXS pattern, with the appearance of the previously mentioned feature, at q = 4.7/nm. Therefore, it seems that in the charge process the formed crystallites are shielded from the surrounding in such a way – possibly with a slowly varying amount of sodiation (and thus no abrupt change in SLD), in order that the overall scattering contrast is little affected. During desodiation, this "continuity" is probably disrupted due to structural reorganization, such that the contrast and thus the scattering become stronger.

Finally, the different behaviour of the SAXS curves during charge and discharge indicate a slow Na diffusion into the a-P/C particles during sodiation and a corresponding faster diffusion during desodiation.

Conclusions

The charge/discharge of an a-P/C anode for SIB has been investigated through a simultaneous combination of SAXS/WAXS. A regular ordering emerging toward the end of the desodiation was observed for the first time on this system with SAXS and could be related to the partial reversibility of the anode. At the same time, this structural reorganization contributes to a stronger scattering contrast. A 2-level Beaucage model was applied to fit the SAXS curves at various stages of sodiation/desodiation and showed a change in fractal dimensions during cycling. This work shows that innovative *operando* measurements can unravel new mechanisms of reactions in the quest of improving the performances of batteries. Furthermore, our proposed set up can be applied to the study of any batteries and can be extremely useful for the detection of self-organized super structures and variation of the morphology of the active material surface.

Supporting Information

Full WAXS pattern of the electrochemical cell and aluminum foil. Sequence of SAXS curves collected during the charge and discharge cycle. SAXS curves of the single components of the electrochemical cell. SEM and EDX images of the electrode.

Acknowledgments

The authors acknowledge NWO and the ESRF for providing beamtime. M. Povia and prof. S. Sartori acknowledge funding from UiO Energy.

Figures

Figure 1. a) Voltage profile of a-P/C cycled between 2 and 0.01 V at C/10 in the *operando* cell. The two arrows indicate the reaction process. The black curve represents the charging process (Na_3P formation) and following the black arrow the reaction move toward the crystalline Na_3P. While the red curve represents the discharge and the red arrow indicate the reverse process, toward the a-P/C re-formation. The specific sodiation capacity is 2000 mAh/g. The obtained reversible specific capacity is 1762 mAh/g. Figures 1b and 1c show the evolution of the diffraction peaks of crystalline Na_3P. Only the peaks (110) and (103) are visible in the d-range 2.5-2.3 Å. During charging (panel b) the diffraction peaks appear from the background at 1732 mAh/g and reach their maximum at the end of the charge at 2000 mAh/g. During the discharge (panel c) the diffraction peak intensity decreases until the peaks disappear completely at 1233 mAh/g.

Figure 2. SAXS profiles of the first (black) and the last measurement (red) of the charge/discharge (sodiation/desodiation) cycle. The black and the red curves do not overlap and two features T and Z appear. The curves in panel b and c are named with the value of the corresponding specific capacity measured in mAh/g. The symbols # and * are used to distinguish the charge and the discharge respectively. T appears from the baseline at 325 mAh/g. It grows until the end of the charge and remains constant until the end of the discharge. The second feature appears towards the end of the desodiation and varies in intensity.

Figure 3. a) Beaucage fit of the first SAXS data collected (black curve in Figure 2a). b) Beaucage fit of data at the end of discharge, red curve in Figure 2a).

Figure 4. a) Power law exponent (fit of $I = k * q^{-\alpha}$) in the low-q region of the SAXS patterns during desodiation. Range used q = 0.17-0.3/nm. b) Apparent volume fraction change during desodiation. The horizontal axis goes from large to small mAh/g values corresponding to the desodiation process.

Figure 5. Changes in area of the feature T (cf. Figure 2) during sodiation.

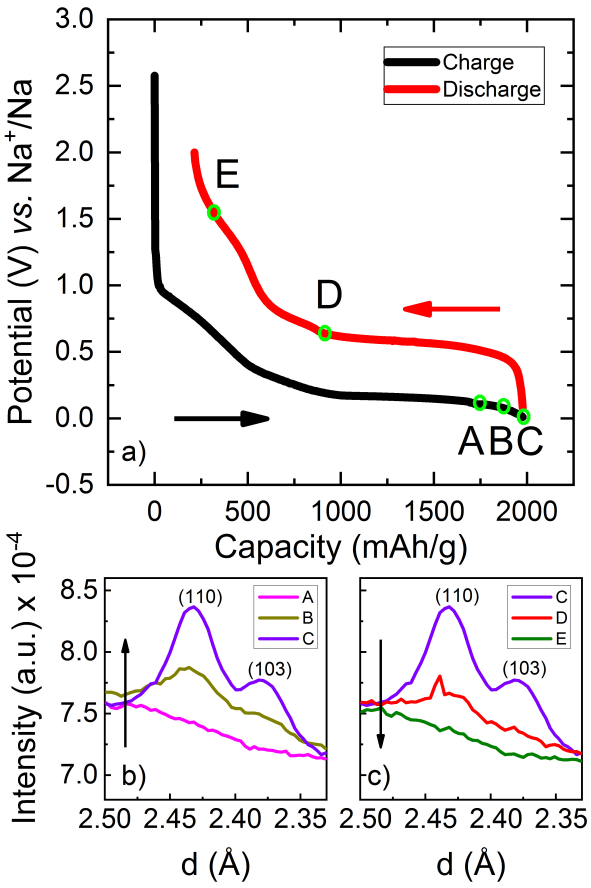

Figure 1

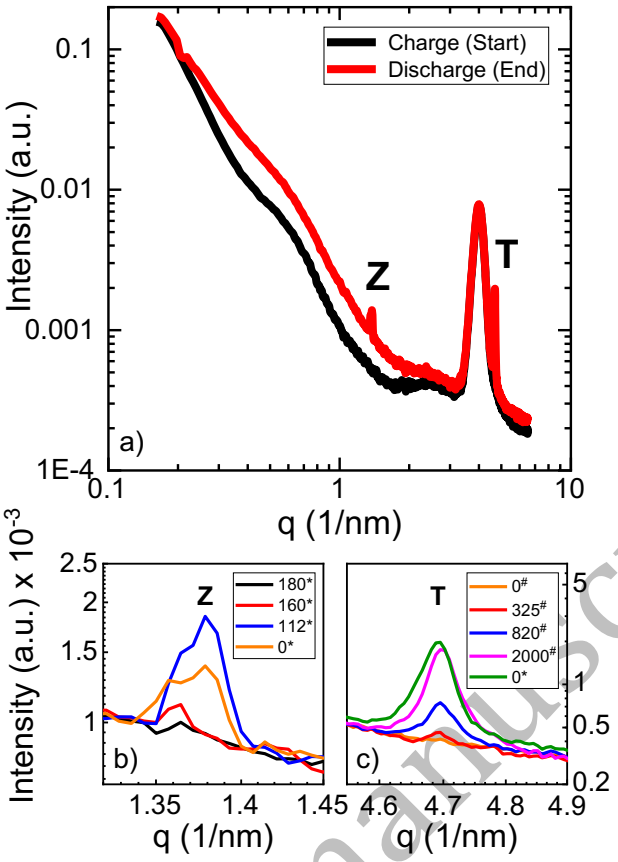

Figure 2

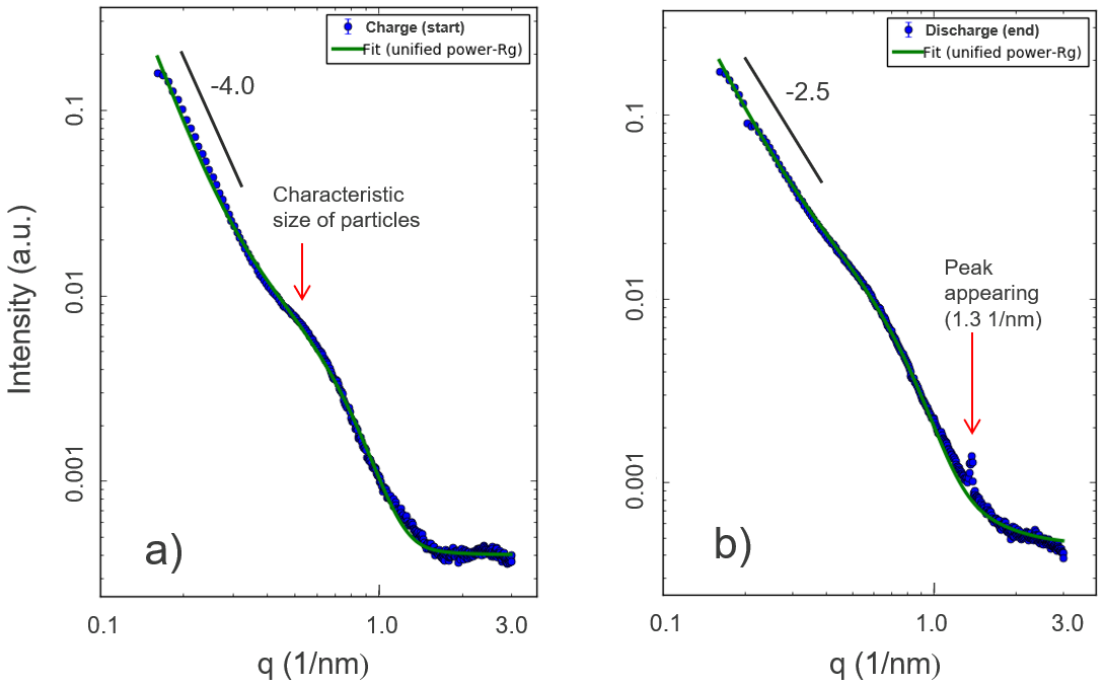

Figure 3

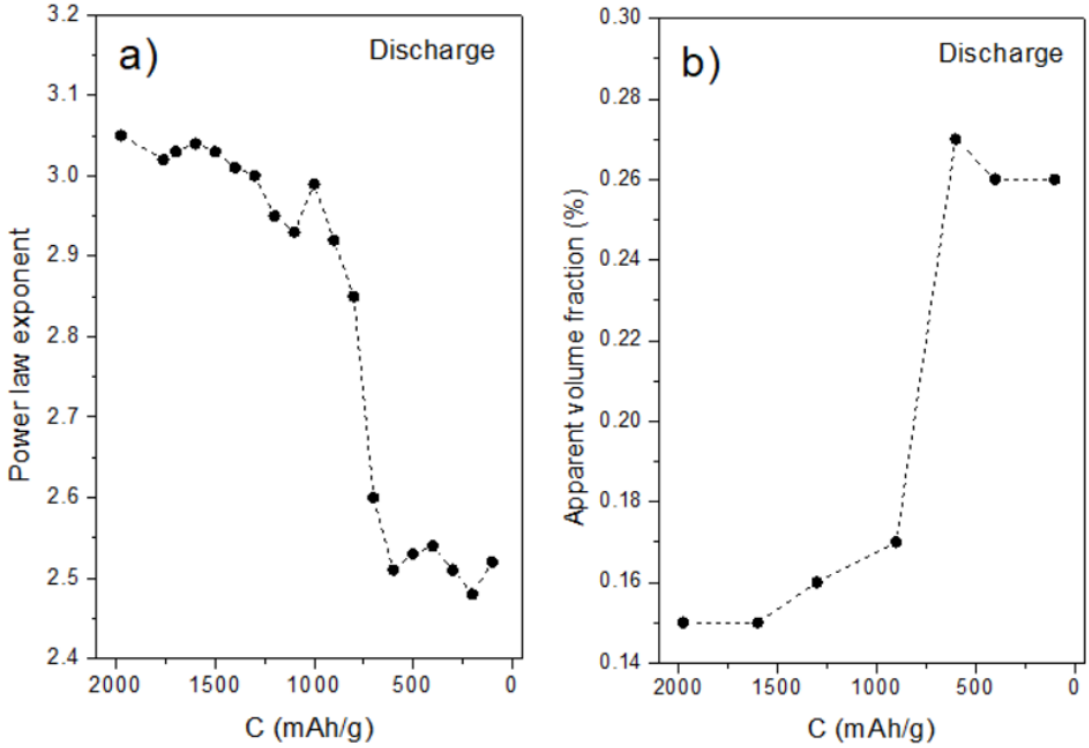

Figure 4

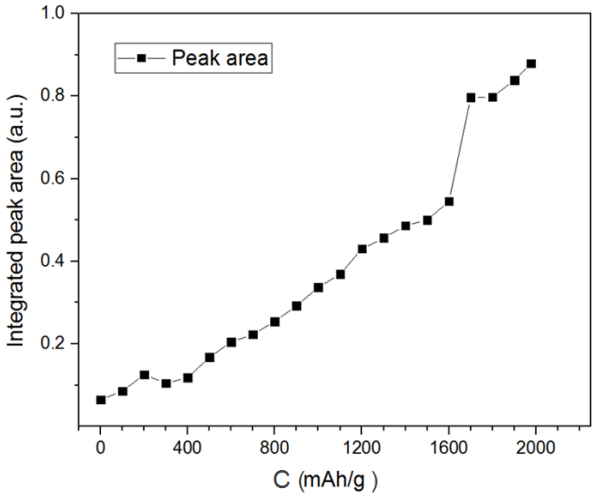

Figure 5

References

(1) Kim, H.; Han, B.; Choo, J.; Cho, J. Three-Dimensional Porous Silicon Particles for Use in High-Performance Lithium Secondary Batteries. *Angew. Chemie - Int. Ed.* **2008**, *47* (52), 10151–10154.

(2) Slater, M. D.; Kim, D.; Lee, E.; Johnson, C. S. Sodium-Ion Batteries. *Adv. Funct. Mater.* **2013**, *23* (8), 947–958.

(3) Pan, H.; Hu, Y.-S.; Chen, L. Room-Temperature Stationary Sodium-Ion Batteries for Large-Scale Electric Energy Storage. *Energy Environ. Sci.* **2013**, *6* (8), 2338–2360.

(4) Jian, Z.; Zhao, B.; Liu, P.; Li, F.; Zheng, M.; Chen, M.; Shi, Y.; Zhou, H. Fe_2O_3 Nanocrystals Anchored onto Graphene Nanosheets as the Anode Material for Low-Cost Sodium-Ion Batteries. *Chem. Commun.* **2014**, *50* (10), 1215–1217.

(5) Xiong, H.; Slater, M. D.; Balasubramanian, M.; Johnson, C. S.; Rajh, T. Amorphous TiO_2 Nanotube Anode for Rechargeable Sodium Ion Batteries. *J. Phys. Chem. Lett.* **2011**, *2* (20), 2560–2565.

(6) Oh, S.; Hwang, J.; Yoon, C. S.; Lu, J.; Amine, K.; Belharouak, I.; Sun, Y. High Electrochemical Performances of Microsphere C-TiO_2 Anode for Sodium-Ion Battery. *Appl. Mater. interface* **2014**, *6* (14), 11295–11301.

(7) Yu, L.; Liu, J.; Xu, X.; Zhang, L.; Hu, R.; Liu, J.; Ouyang, L.; Yang, L.; Zhu, M. Ilmenite Nanotubes for High Stability and High Rate Sodium-Ion Battery Anodes. *ACS Nano* **2017**, *11* (5), 5120–5129.

(8) Sun, N.; Liu, H.; Xu, B. Facile Synthesis of High Performance Hard Carbon Anode Materials for Sodium Ion Batteries. *J. Mater. Chem. A* **2015**, *3* (41), 20560–20566.

(9) Wang, J.; Luo, C.; Mao, J.; Zhu, Y.; Fan, X.; Gao, T.; Mignerey, A. C.; Wang, C. Solid-State Fabrication of SnS_2/C Nanospheres for High-Performance Sodium Ion Battery Anode. *Appl. Mater. interface* **2015**, *7* (21), 11476–11481.

(10) Xiao, L.; Cao, Y.; Xiao, J.; Wang, W.; Kovarik, L.; Nie, Z.; Liu, J. High Capacity, Reversible Alloying Reactions in SnSb/C Nanocomposites for Na-Ion Battery Applications. *Chem. Commun.* **2012**, *48* (27), 3321–3323.

(11) Baggetto, L.; Hah, H.-Y.; Johnson, C. E.; Bridges, C. A.; Johnson, J. A.; Veith, G. M. The Reaction Mechanism of $FeSb_2$ as Anode for Sodium-Ion Batteries.

Phys. Chem. Chem. Phys. **2014**, *16* (20), 9538–9545.

(12) Alcántara, R.; Jiménez-Mateos, J. M.; Lavela, P.; Tirado, J. L. Carbon Black: A Promising Electrode Material for Sodium-Ion Batteries. *Electrochem. commun.* **2001**, *3* (11), 639–642.

(13) Hu, Z.; Wang, L.; Zhang, K.; Wang, J.; Cheng, F.; Tao, Z.; Chen, J. MoS2 Nanoflowers with Expanded Interlayers as High-Performance Anodes for Sodium-Ion Batteries. *Angew. Chemie - Int. Ed.* **2014**, *53* (47), 12794–12798.

(14) Zhu, C.; Mu, X.; Vanaken, P. A.; Yu, Y.; Maier, J. Single-Layered Ultrasmall Nanoplates of MoS2 Embedded in Carbon Nanofibers with Excellent Electrochemical Performance for Lithium and Sodium Storage. *Angew. Chemie - Int. Ed.* **2014**, *53* (8), 2152–2156.

(15) Legrain, F.; Sottmann, J.; Kotsis, K.; Gorantla, S.; Sartori, S.; Manzhos, S. Amorphous (Glassy) Carbon, a Promising Material for Sodium Ion Battery Anodes: A Combined First-Principles and Experimental Study. *J. Phys. Chem. C* **2015**, *119* (24), 13496–13501.

(16) Qian, J.; Wu, X.; Cao, Y.; Ai, X.; Yang, H. High Capacity and Rate Capability of Amorphous Phosphorus for Sodium Ion Batteries. *Angew. Chemie - Int. Ed.* **2013**, *52* (17), 4633–4636.

(17) Kim, Y.; Park, Y.; Choi, A.; Choi, N. S.; Kim, J.; Lee, J.; Ryu, J. H.; Oh, S. M.; Lee, K. T. An Amorphous Red Phosphorus/carbon Composite as a Promising Anode Material for Sodium Ion Batteries. *Adv. Mater.* **2013**, *25* (22), 3045–3049.

(18) Song, J.; Yu, Z.; Gordin, M. L.; Li, X.; Peng, H.; Wang, D. Advanced Sodium Ion Battery Anode Constructed via Chemical Bonding between Phosphorus, Carbon Nanotube, and Cross-Linked Polymer Binder. *ACS Nano* **2015**, *9* (12), 11933–11941.

(19) Dong, Y.; Disalvo, F. J. Reinvestigation of Na3P Based on Single-Crystal Data. *Acta Crystallogr. Sect. E* **2005**, *61* (11), 3–8.

(20) Gershinsky, G.; Bar, E.; Monconduit, L.; Zitoun, D. Operando Electron Magnetic Measurements of Li-Ion Batteries. *Energy Environ. Sci.* **2014**, *7* (6), 2012–2016.

(21) Tepavcevic, S.; Xiong, H.; Stamenkovic, V. R.; Zuo, X.; Balasubramanian, M.; Prakapenka, V. B.; Johnson, C. S.; Rajh, T. Nanostructured Bilayered Vanadium Oxide Electrodes for Rechargeable Sodium-Ion Batteries. *ACS*

Nano **2012**, *6* (1), 530–538.

(22) Sottmann, J.; Homs-Regojo, R.; Wragg, D. S.; Fjellvåg, H.; Margadonna, S.; Emerich, H. Versatile Electrochemical Cell for Li/Na-Ion Batteries and High-Throughput Setup for Combined Operando X-Ray Diffraction and Absorption Spectroscopy. *J. Appl. Crystallogr.* **2016**, *49* (6), 1972–1981.

(23) Sandì, G.; Joachin, H.; Kizilel, R.; Carrado, K. A. In Situ SAXS Studies of the Structural Changes of Polymer Nanocomposites Used in Battery Applications. *Chem. Mater.* **2003**, *15* (4), 838–843.

(24) Portale, G.; Cavallo, D.; Alfonso, G. C.; Hermida-Merino, D.; van Drongelen, M.; Balzano, L.; Peters, G. W. M.; Goossens, J. G. P.; Bras, W. Polymer Crystallization Studies under Processing-Relevant Conditions at the SAXS/WAXS DUBBLE Beamline at the ESRF. *J. Appl. Crystallogr.* **2013**, *46* (6), 1681–1689.

(25) Bras, W.; Dolbnya, I. P.; Detollenaere, D.; van Tol, R.; Malfois, M.; Greaves, G. N.; Ryan, A. J.; Heeley, E. Recent Experiments on a Small-Angle/Wide-Angle X-Ray Scattering Beam Line at the ESRF. *J. Appl. Crystallogr.* **2003**, *36* (3 Part 1), 791–794.

(26) Hammersley, A. P.; Svensson, S. O.; Hanfland, M.; Fitch, A. N.; Hausermann, D. Two-Dimensional Detector Software: From Real Detector to Idealised Image or Two-Theta Scan. *High Press. Res.* **1996**, *14* (4–6), 235–248.

(27) Larcher, D.; Beattie, S.; Morcrette, M.; Edström, K.; Jumas, J.-C.; Tarascon, J.-M. Recent Findings and Prospects in the Field of Pure Metals as Negative Electrodes for Li-Ion Batteries. *J. Mater. Chem.* **2007**, *17* (36), 3759–3772.

(28) Obrovac, M. N.; Chevrier, V. L. Alloy Negative Electrodes for Li-Ion Batteries. *Chem. Rev*. 2014, pp 11444–11502.

(29) Komaba, S.; Shimomura, K.; Yabuuchi, N.; Ozeki, T.; Yui, H.; Konno, K. Study on Polymer Binders for High-Capacity SiO Negative Electrode of Li-Ion Batteries. *J. Phys. Chem. C* **2011**, *115* (27), 13487–13495.

(30) Koo, B.; Kim, H.; Cho, Y.; Lee, K. T.; Choi, N. S.; Cho, J. A Highly Cross-Linked Polymeric Binder for High-Performance Silicon Negative Electrodes in Lithium Ion Batteries. *Angew. Chemie - Int. Ed.* **2012**, *51* (35), 8762–8767.

(31) Sangster, J. M. Na-P (Sodium-Phosphorus) System. *J. Phase Equilibria Diffus.* **2010**, *31* (1), 62–67.

(32) Sottmann, J.; Michiel, M. Di; Fjellv, H.; Malavasi, L.; Margadonna, S.;

Vajeeston, P.; Vaughan, G. B. M.; Wragg, D. S. Sodium Ion Batteries Chemical Structures of Specific Sodium Ion Battery Components Determined by Operando Pair Distribution Function and X-Ray Diffraction Computed Tomography. *Angew. Chemie - Int. Ed.* **2017**, *56* (38), 11385–11389.

(33) Beaucage, G.; Kammler, H. K.; Pratsinis, S. E. Particle Size Distributions from Small-Angle Scattering Using Global Scattering Functions. *J. Appl. Crystallogr.* **2004**, *37* (4), 523–535.

(34) Butler, P.; Doucet, M.; Jackson, A.; King, S. SAS view http://www.sasview.org/.

(35) Glatter, O.; Kratky, O. *Small Angle X-Ray Scattering*; Academic press, 1982.

(36) Rudola, A.; Aurbach, D.; Balaya, P. A New Phenomenon in Sodium Batteries : Voltage Step due to Solvent Interaction. *Electrochem. commun.* **2014**, *46*, 56–59.

(37) Dugas, R.; Ponrouch, A.; Gachot, G.; David, R.; Palacin, M. R. Na Reactivity toward Carbonate-Based Electrolytes : The Effect of FEC as Additive. **2016**, *163* (10), 2333–2339.

TOC Graphic